

# Solutions for Incompressible Viscous Flow in a Triangular Cavity using Cartesian Grid Method

B. M. Pasquim<sup>1</sup> and V. C. Mariani<sup>2</sup>

**Abstract:** This study presents a Cartesian grid method and its application to solve a steady flow in a lid-driven triangular two-dimensional cavity. The evolution of stream function and vorticity inside a triangular lid-driven cavity, when the Reynolds number changes from 1 to 6000, is presented. For space discretization on the interior of triangular cavity orthogonal Cartesian grid is used. Then, using this grid, trapezoidal volumes appear in the interface between solid and fluid. For a suitable treatment of these volumes the Eulerian-Lagrangian methodology is used. The Navier-Stokes equations are solved numerically using finite-volume method. On the basis of the numerical studies reported here it seems that the method under investigation has no difficulty at capturing the formation of primary, secondary and tertiary vortices as Reynolds number increases. It is observed also that the interior of the primary vortex has almost constant stream function and vorticity for reasonably large Reynolds number. Highly accurate benchmark results are provided including new global quantities as the kinetic energy and the enstrophy.

**Keyword:** Triangular cavity, Cartesian grid, Eulerian-Lagrangian methodology, finite-volume method

## 1 Introduction

The flow of a fluid in lid-driven cavities is a problem of primary importance in computational fluid dynamics. The development of improved methods to solve these problems has also been a subject of concern to computational physicists for many years. The representation of cavities of square section with infinite axial length, bidimensional cavities, has been widely studied and is now a standard case test for new computational schemes. Benjamin and Denny (1979), Ghia et al. (1982),

---

<sup>1</sup> Department of Chemical Engineering, Pontifical Catholic University of Paraná, Rua Imaculada Conceição, 1155, Prado Velho, 80215-901, Curitiba, PR, Brazil.

<sup>2</sup> Department of Mechanical Engineering, Pontifical Catholic University of Paraná, Rua Imaculada Conceição, 1155, Prado Velho, 80215-901, Curitiba, PR, Brazil. {viviana.mariani@pucpr.br}

Botella and Peyret (1998), and Bruneau and Saad (2006), are some of the many existing works. They employed finite-difference method with stream function-vorticity formulation, except the last author, that used uniform Cartesian meshes.

Some recent studies solving flows in lid-driven cavities have used meshless methods. One popular method is the meshless local Petrov-Galerkin (MLPG) successfully used by Lin and Atluri (2001), and Ahrem et al. (2006). Arefmanesh et al. (2008) applied a MLPG for the solution of the Navier-Stokes equations for the non-isothermal lid-driven cavity flow and other problems. Tsai et al. (2002) developed a meshless boundary elements method to solve 3D Stokes flows. The iterative process used in that study is similar to the process employed in Nicolás and Bermúdez (2007), the only difference is that these use a truly fixed point one, with a different discretization time, while Nicolás and Bermúdez (2004) studied the 2D flows.

Radial basis functions (RBFs) are a powerful tool for function interpolation. Due to their mesh-free nature RBFs have received an increasing attention for solving partial differential equations. The trial of such exploration was made by Atluri et al. (2006a, 2006b), Han et al. (2006), Wen and Hon (2007), Mai-Duy et al. (2007).

Another method is Multiquadric Collocation Method (MCM) using radial basis function that has been used in a variety of works between them the lid-driven cavity flows. For example, Ding et al. (2006) used MCM to solve the three-dimensional lid-driven cavity flow problem. Young et al. (2004) solved the Stokes flow problem in cavity by MCM. Chantasiriwan (2006) reports driven cavity results for the low Reynolds numbers  $Re = 0$ , which turns out to be a Stokes flow because of its infinity viscosity, and  $Re = 100$  using a MCM. Mai-Duy and Tran-Cong (2004) with the primitive variables formulation, report also the lid-driven cavity flow for  $Re = 100$  and  $Re = 0$ , where  $Re$  is the Reynolds number. Grimaldi et al. (2006) using a parallel multi-block method reported results for 2D and 3D lid-driven cavity problem. In Orsini et al. (2008) was presented a modified control volume method using a radial basis function interpolation to improve the prediction of the flux accuracy at the faces of the control volumes. The proposed approach validated a series de 1D and 3D test cases. Shan et al. (2008) numerically study the performance of the 3D local multiquadric-based differential quadrature (MQ-DQ) method and demonstrate its capability and flexibility for simulation of 3D incompressible fluid flows with curved boundary. A new meshless approach was proposed by Mai-Cao and Tran-Cong (2008) to solving a special class of moving interface problems. Sellountos and Sequeira (2008) proposed a hybrid velocity-vorticity scheme for the solution of the 2D Navier-Stokes equations. Mariani et al. (2008) investigated unstructured meshes of Voronoi to solve flow in square lid-driven cavities.

In fact, a variety of numerical methods are used to solve the flow in square cavity with one side translating with uniform velocity – finite difference, false tran-

sients, finite elements, finite volume, spectral, multigrid, meshless methods, etc. It is generally agreed that there is a dominant recirculation whose center is closer to the moving wall. As the Reynolds number is increasing, this center first moves downstream, then moves towards the middle of the enclosure. There are two small counter recirculating vortices at the stagnant corners. The vorticity is most intense near of moving boundary. For high Reynolds number the vorticity is confined to a boundary layer and the interior vorticity is approximately constant (Ribbens et al., 1994).

In irregular cavities, such as trapezoidal, semi-circular or triangular cavities, special attention has been give to boundaries, i.e., for example, the classic finite-volume method, using structured meshes, should be changed to solve the flow in these geometries. These differences promote the development of the searches and of new numerical methods each time more fast and accurate for the solution of flows in irregular geometries.

In literature there are some studies of flow in curved and nonrectangular cavities. The triangular cavity exhibits flow features that have been analytically studied by Moffat (1963) in the Stokes regime and by Batchelor (1956) in the inviscid or infinite Reynolds number regime. The flow in a trapezoidal cavity was studied by Darr and Vanka (1991). Ribbens et al. (1991) described the flow in an elliptic region with a moving boundary. McQuain et al. (1994) and Ribbens et al. (1994) studied the steady flow in an equilateral triangular cavity for  $Re \leq 500$ . The fourth-order Navier-Stokes equations in terms of stream function were solved numerically using finite differences together with a Newton-like iteration on a transformed geometry. Vynnycky and Kimura (1994) reported the results of their study about steady flow in a driven quarter circular cavity.

Jyotsna and Vanka (1995) studied the steady viscous flow in a triangular cavity, where was used triangular grids and a multigrid method. The solution for  $Re \leq 800$  was obtained without encountering any of the difficulties reported for structured grid-based methods in Ribbens et al. (1994). Li and Tang (1996) presented an accurate and efficient numerical method to solve the flow in equilateral and scalene triangular cavities for  $Re \leq 1500$ , such method using finite difference on a transformed geometry. Recently, Glowinski et al. (2006) reported the results of their study of incompressible viscous flow in a semi-circular cavity. The operator-splitting/finite elements and a triangulation of the two-dimensional domain were used to obtain numerical results. The Lattice Boltzmann method was investigated by Duan and Liu (2007) to solve triangular cavity flow for  $Re \leq 500$ .

In fact, the flow in curved geometries can be represented using curvilinear and non orthogonal grids or orthogonal (Cartesian) grids. In this context, the our primary goal here is to investigate the ability of the finite volume/Eulerian-Lagrangian tech-

nique using Cartesian grids as discussed in Ye et al. (1999), and Mariani and Prata (2008) at handling flow regions with corners and curved boundaries. To achieve the goal above, we selected a wall-driven triangular cavity flow. This problem is important and interesting because triangular shape is at least as common in practice as the square shape, also to see what aspects the results of this problem will differ from those of the previous one. A secondary goal is to determine the structure of the recirculating flow for Reynolds number in the range between 1 and 6000, corresponding to Reynolds number much upper than those considered in previous studies.

The paper is organized as follows. Section 2 introduces the formulation of the problem and shows the space discretization of governing equations in Cartesian grid. Numerical results are presented in Section 3, including a comparison with some results presented in Li and Tang (1996) and McQuain et al. (1994). Streamlines and contours of vorticity are presented to  $Re \leq 6000$  in the same section. In the last section the main conclusions are described.

## 2 Problem Formulation

Figure 1 shows the geometry of the triangular cavity, with the coordinate system used here. Thus, a steady, incompressible viscous fluid fills a triangular cavity, see Fig. 1. The domain occupied by the fluid is then a two-dimensional region, and its flow is governed by the Navier-Stokes equations,

$$\frac{\partial u}{\partial x} + \frac{\partial v}{\partial y} = 0, \quad (1)$$

$$\frac{\partial(uu)}{\partial x} + \frac{\partial(vu)}{\partial y} = -\frac{\partial p}{\partial x} + \nu \left[ \frac{\partial^2 u}{\partial x^2} + \frac{\partial^2 u}{\partial y^2} \right] \quad (2)$$

$$\frac{\partial(uv)}{\partial x} + \frac{\partial(vv)}{\partial y} = -\frac{\partial p}{\partial y} + \nu \left[ \frac{\partial^2 v}{\partial x^2} + \frac{\partial^2 v}{\partial y^2} \right] \quad (3)$$

where  $u$  (m/s) and  $v$  (m/s) are velocity components in the  $x$  and  $y$  directions, respectively,  $\nu$  ( $m^2/s$ ) e  $\rho$  ( $kg/m^3$ ) are the dynamics viscosity and density, respectively, and  $p$  (Pa) is the pressure.

The boundary conditions for triangular cavity, illustrated in Fig. 1, are given by:

- (i)  $u = 1, v = 0$  for  $y = H$  and  $0 \leq x \leq L$ ;
- (ii)  $u = 0, v = 0$  for  $y = f(x) = -\sqrt{3}x + 3$  and  $0 \leq x \leq L/2$ .
- (iii)  $u = 0, v = 0$  for  $y = f(x) = \sqrt{3}x - 3$  and  $L/2 < x \leq L$ .

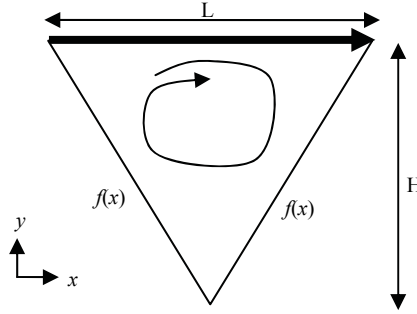


Figure 1: Triangular cavity.

The lid-driven triangular cavity illustrated in Fig. 1 has the dimensions  $L = 2\sqrt{3}$  m and  $H = 3$  m, generating an equilateral cavity with length of each side  $2\sqrt{3}$  m.

As a common practice Eqs. (1) to (3) can be expressed by a single equation for the generic variable  $\phi$  as

$$\frac{\partial(\rho u \phi)}{\partial x} + \frac{\partial(\rho v \phi)}{\partial y} = \Gamma^\phi \frac{\partial}{\partial x} \left( \frac{\partial \phi}{\partial x} \right) + \Gamma^\phi \frac{\partial}{\partial y} \left( \frac{\partial \phi}{\partial y} \right) + S^\phi, \quad (4)$$

where  $\phi$  is equal to  $u$  and  $v$  for Eqs. (2) and (3), respectively, and equal to unity for Eq. (1), and  $\Gamma^\phi$  and  $S^\phi$  are, respectively, the diffusion coefficient and term source. The governing equation, Eq. (4), will be discretized first in the full cells, cells located inside of domain, and to follow the discretization will be presented for trapezoidal cells, located in domain boundaries.

### 2.1 Discretization for full cells

The Eq. (4) with their respective boundary conditions is solved here using the finite-volume method described by Patankar (1980). The triangular cavity is divided into small no overlapping rectangular control volumes, i.e., the equation is discretized on a Cartesian grid using a collocated (non-staggered) arrangement of the primitive variables which are collocated at the cell-center. Integrating the Eq. (4) over a typical control volume in the fluid domain, such as presented in Fig. 2, yields,

$$\int_s^n \int_I^e \frac{\partial(\rho u \phi)}{\partial x} dx dy + \int_I^e \int_s^n \frac{\partial(\rho v \phi)}{\partial y} dy dx = \int_s^n \int_I^e \Gamma^\phi \frac{\partial^2 \phi}{\partial x^2} dx dy + \int_I^e \int_s^n \Gamma^\phi \frac{\partial^2 \phi}{\partial y^2} dy dx + \bar{S}^\phi \quad (5)$$

where the lower subscripts  $e$ ,  $w$ ,  $n$  and  $s$  indicate the values at the cell faces east, west, north, and south of the control volume, respectively, as shown in Fig. 2.

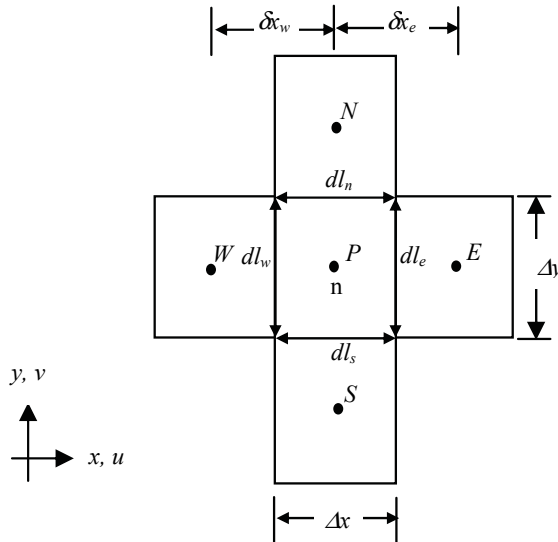


Figure 2: Full cell.

The Eq. (5) can be rewritten as,

$$\begin{aligned}
 &(\rho u \phi dl)_e - (\rho u \phi dl)_w + (\rho v \phi dl)_n - (\rho v \phi dl)_s \\
 &= \bar{S}^\phi + \left( \Gamma_e^\phi \frac{\partial \phi}{\partial x} \right)_e dl_e - \left( \Gamma_w^\phi \frac{\partial \phi}{\partial x} \right)_w dl_w + \left( \Gamma_n^\phi \frac{\partial \phi}{\partial y} \right)_n dl_n - \left( \Gamma_s^\phi \frac{\partial \phi}{\partial y} \right)_s dl_s. \quad (6)
 \end{aligned}$$

Substituting convective and total fluxes represented by  $F = (\rho \mathbf{u} dl)$  and  $J = [\rho \mathbf{u} \phi - \Gamma^\phi (\partial \phi / \partial n)] dl$ , respectively, and now multiplying the discrete continuity equation by the value  $\phi_P$  and subtracting from Eq. (6) gives

$$(J_e - F_e \phi_P) - (J_w - F_w \phi_P) + (J_n - F_n \phi_P) - (J_s - F_s \phi_P) = \bar{S}^\phi \quad (7)$$

Thus, the algebraic equation for the control volume  $P$  can be expressed as

$$\begin{aligned}
 a_P \phi_P &= a_E \phi_E + a_W \phi_W + a_N \phi_N + a_S \phi_S + \bar{S}^\phi \\
 a_E &= D_e A |P_e| + \langle -F_e, 0 \rangle \\
 a_W &= D_w A |P_w| + \langle F_w, 0 \rangle \\
 a_N &= D_n A |P_n| + \langle -F_n, 0 \rangle \\
 a_S &= D_s A |P_s| + \langle F_s, 0 \rangle \\
 a_P &= a_E + a_W + a_N + a_S \\
 \bar{S}^\phi &= \begin{cases} -p_e dl_e + p_w dl_w, & \text{if } \phi = u, \\ -p_n dl_n + p_s dl_s, & \text{if } \phi = v, \end{cases}
 \end{aligned} \tag{8}$$

in which  $\langle a, b \rangle$  is a function that stands for the largest of the quantities  $a$  or  $b$ ,  $A|P| = \langle 0, (1 - 0, 1|P|)^5 \rangle$  is the Power-Law scheme employed to discretize spatial derivatives (Patankar, 1980), and  $P = F/D$  is the cell Peclet number.

## 2.2 Discretization for trapezoidal cells

This work uses marker particles to identify the intersection of the interfacial function,  $f(x)$ , which defines the solid boundary, with the Cartesian fix grid. Marker particles have been used for more than four decades (Peskin, 1977), and are attractive due to their ability to model interfaces with complex topologies. A detailed presentation of an Eulerian method (fixed grid) used in combination with a Lagrangian method (interface tracking) as employed here, can be found elsewhere Udaykumar *et al.* (1996), Shyy *et al.* (1996), Ye *et al.* (1999) and Mariani and Prata (2008).

The cut cells on the vicinity of a solid boundary passing through the Cartesian grid are irregularly shaped. In this study there are six possibilities for interfacial volumes, see Fig. 3. However, only the discretization of a typical interfacial control volume will be presented in details. An interpolation function developed for the cells cut by irregular boundaries, which preserves the second-order spatial accuracy and conservation properties of the solver, was taken from (Ye *et al.*, 1999). The typical interfacial volume to be explored in discretizing of the general governing equation is illustrated in Fig. 3a.

Integration of Eq. (4) over an interfacial control volume in fluid domain, such as

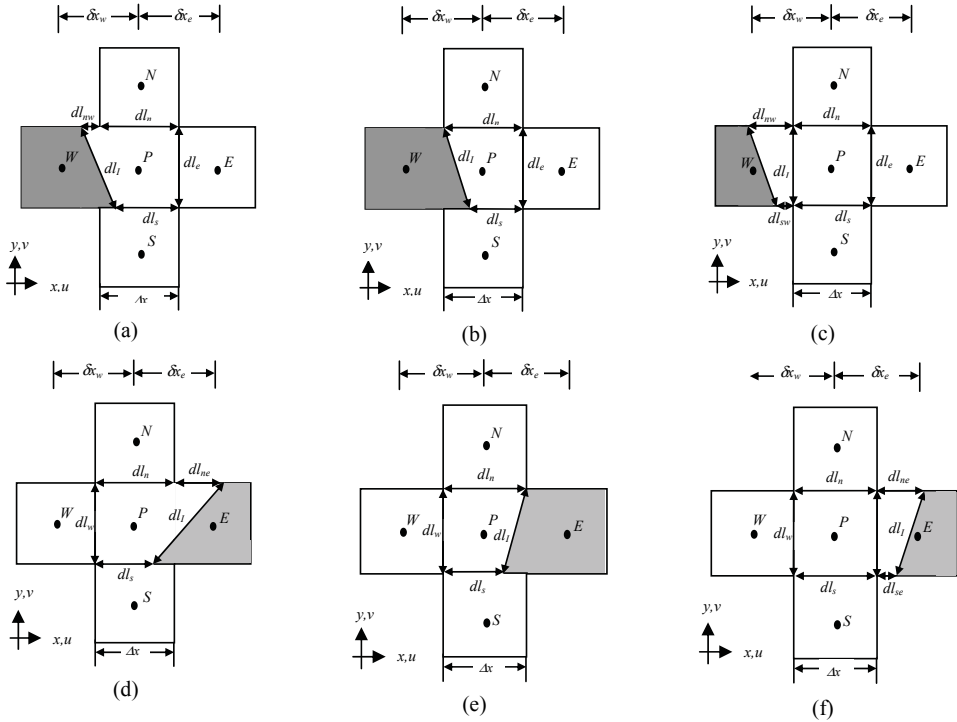


Figure 3: Trapezoidal cells (a) first, (b) second, (c) third, (d) fourth, (e) fifth, and (f) sixth types..

the one presented in Fig. 3a, yields,

$$\int_s^{n,nw} \int_I^e \frac{\partial(\rho u \phi)}{\partial x} dx dy + \int_I^e \int_s^{n,nw} \frac{\partial(\rho v \phi)}{\partial y} dy dx = \int_s^{n,nw} \int_I^e \Gamma^\phi \frac{\partial^2 \phi}{\partial x^2} dx dy + \int_I^e \int_s^{n,nw} \Gamma^\phi \frac{\partial^2 \phi}{\partial y^2} dy dx + \bar{S}^\phi \quad (9)$$

After of integration of the Eq. (9) yields,

$$\begin{aligned} & (\rho u \phi)_e dl_e - (\rho u_n \phi)_I dl_I + (\rho v \phi)_n dl_n + (\rho v \phi)_{nw} dl_{nw} - (\rho v \phi)_s dl_s \\ & = \bar{S}^\phi + \Gamma_e^\phi \left( \frac{\partial \phi}{\partial x} \right)_e dl_e - \Gamma_I^\phi \left( \frac{\partial \phi}{\partial n} \right)_I dl_I + \Gamma_n^\phi \left( \frac{\partial \phi}{\partial y} \right)_n dl_n + \Gamma_{nw}^\phi \left( \frac{\partial \phi}{\partial y} \right)_{nw} dl_{nw} \\ & \quad - \Gamma_s^\phi \left( \frac{\partial \phi}{\partial y} \right)_s dl_s, \quad (10) \end{aligned}$$

Replacing the convective fluxes and multiplying the discrete continuity equation by the value  $\phi_P$  and subtracting from Eq. (10) gives

$$\begin{aligned}
 & F_e(\phi_e - \phi_P) - F_I(\phi_I - \phi_P) + F_n(\phi_n - \phi_P) + F_{nw}(\phi_{nw} - \phi_P) - F_s(\phi_s - \phi_P) \\
 &= \bar{S}^\phi + \Gamma_e^\phi \left( \frac{\partial \phi}{\partial x} \right)_e dl_e - \Gamma_I^\phi \left( \frac{\partial \phi}{\partial n} \right)_I dl_I + \Gamma_n^\phi \left( \frac{\partial \phi}{\partial y} \right)_n dl_n + \Gamma_{nw}^\phi \left( \frac{\partial \phi}{\partial y} \right)_{nw} dl_{nw} \\
 & \quad - \Gamma_s^\phi \left( \frac{\partial \phi}{\partial y} \right)_s dl_s. \quad (11)
 \end{aligned}$$

Here the  $F$ 's stand for the mass fluxes through the faces of the control volume. Subscript  $I$  indicates the values at the interface. The manner in which these fluxes are evaluated determines the order of accuracy of the scheme employed. In this study  $\phi_I$  and  $F_I$  are nulls. Substituting the total flux the Eq. (11) can be written as

$$(J_e - F_e \phi_P) + (J_n - F_n \phi_P) = \bar{S}^\phi - (J_{nw} - F_{nw} \phi_P) + (J_s - F_s \phi_P) - \Gamma_I^\phi \left( \frac{\partial \phi}{\partial n} \right)_I dl_I, \quad (12)$$

or

$$\begin{aligned}
 a_P \phi_P &= a_E \phi_E + a_N \phi_N + b^\phi \\
 a_E &= D_e A(|P_e|) + \langle -F_e, 0 \rangle \\
 a_N &= D_n A(|P_n|) + \langle -F_n, 0 \rangle \\
 a_P &= a_E + a_N \\
 b^\phi &= \bar{S}^\phi - (J_{nw} - F_{nw} \phi_P) + (J_s - F_s \phi_P) - \Gamma_I^\phi \left( \frac{\partial \phi}{\partial n} \right)_I dl_I \\
 \bar{S}^\phi &= \begin{cases} -p_e dl_e + p_I dl_I n_x, & \text{if } \phi = u \\ -p_n dl_n - p_{nw} dl_{nw} + p_s dl_s n_y, & \text{if } \phi = u \end{cases} \quad (13)
 \end{aligned}$$

The variables  $\phi_{nw}$  and  $\partial \phi / \partial y)_{nw}$  are computed using a two-dimensional polynomial interpolating function that is quadratic in  $x$  and linear in  $y$ , in conformity with Ye *et al.* (1999), and Mariani and Prata (2008). An similar interpolation procedure is also used to estimate the values of  $\phi_s$  and  $\partial \phi / \partial y)_s$ . For example, in order to approximate  $\phi_{nw}$ ,  $\phi$  is express in the trapezoidal region shown in Fig. 4a in terms of a function that is linear in  $y$  and quadratic in  $x$

$$\phi_{nw} = c_1 x_{nw}^2 y_{nw} + c_2 x_{nw}^2 + c_3 x_{nw} y_{nw} + c_4 x_{nw} + c_5 y_{nw} + c_6, \quad (14)$$

where each of the unknown coefficients,  $c_1$  to  $c_6$ , are expressed in terms of the

values of  $\phi$  at the six grid points shown in Fig. 4a, expressed in the form of

$$\begin{cases} \phi_{I,1} = c_1 y_{I,1} x_{I,1}^2 + c_2 x_{I,1}^2 + c_3 y_{I,1} x_{I,1} + c_4 x_{I,1} + c_5 y_{I,1} + c_6 \\ \phi_P = c_1 y_P x_P^2 + c_2 x_P^2 + c_3 y_P x_P + c_4 x_P + c_5 y_P + c_6 \\ \phi_E = c_1 y_E x_E^2 + c_2 x_E^2 + c_3 y_E x_E + c_4 x_E + c_5 y_E + c_6 \\ \phi_N = c_1 y_N x_N^2 + c_2 x_N^2 + c_3 y_N x_N + c_4 x_N + c_5 y_N + c_6 \\ \phi_{NW} = c_1 y_{NW} x_{NW}^2 + c_2 x_{NW}^2 + c_3 y_{NW} x_{NW} + c_4 x_{NW} + c_5 y_{NW} + c_6 \\ \phi_{I,2} = c_1 y_{I,2} x_{I,2}^2 + c_2 x_{I,2}^2 + c_3 y_{I,2} x_{I,2} + c_4 x_{I,2} + c_5 y_{I,2} + c_6 \end{cases} \quad (15)$$

The equation system shown in Eq. (15) is solved through of a direct method with partial pivoting.

The value of  $\partial\phi/\partial y)_{nw}$  is expressed as

$$(\partial\phi/\partial y)_{nw} = c_1 x_{nw}^2 + c_3 x_{nw} + c_5, \quad (16)$$

The diffusive flux in the solid-fluid interface can be decomposed as  $(\partial\phi/\partial n)_I = (\partial\phi/\partial x)_I \hat{n}_x + (\partial\phi/\partial y)_I \hat{n}_y$ , where  $\hat{n}_x$  and  $\hat{n}_y$  are the two components of the unit vector normal to interface. Therefore computation of the normal flux requires estimation of  $\partial\phi/\partial x$  and  $\partial\phi/\partial y$  at the center of the interface. For the cell being considered here,  $\partial\phi/\partial x$  is computed to second-order accuracy with relative ease by expressing the  $\phi$  variation along the horizontal line in terms of a quadratic function in  $x$  as follows,

$$\phi = c_1 x^2 + c_2 x + c_3, \quad (17)$$

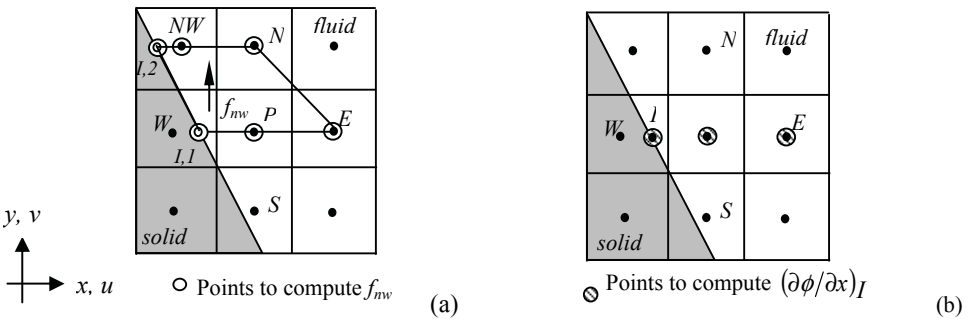


Figure 4: Points used in computation of (a)  $f_{nw}$  e (b)  $(\partial\phi/\partial x)_I$ .

The coefficients in the quadratic function can be expressed in terms of the values of  $\phi$  at the three points indicated in Fig. 4b. Thus, the normal derivative at the center of the interface is evaluated as,

$$\partial\phi/\partial x)_I = 2c_1x_I + c_2, \tag{18}$$

The calculation of  $\partial\phi/\partial y)_I$  for this cell is obtained with similar interpolation used for  $\partial\phi/\partial y)_{nw}$  and  $\partial\phi/\partial y)_s$ , in this context consider the six points illustrated in trapezoid shown in Fig. 5,  $\phi$  is express in terms of a function that is linear in  $y$  and quadratic in  $x$

$$\phi = c_1x^2y + c_2x^2 + c_3xy + c_4x + c_5y + c_6, \tag{19}$$

The value of  $\partial\phi/\partial y)_I$  is expressed deriving the Eq. (19)

$$\partial\phi/\partial y)_I = c_1x_I^2 + c_3x_I + c_5 \tag{20}$$

The fluxes  $f_n$  and  $f_e$ , in the first cell, do no need of special treatment because its faces were not intercepted by interfacial function. In general, there are also interfacial volumes which have an east and west face-cut cell. To evaluate the face flux of those volumes, the interpolation function employed is linear in  $x$  and quadratic in  $y$ .

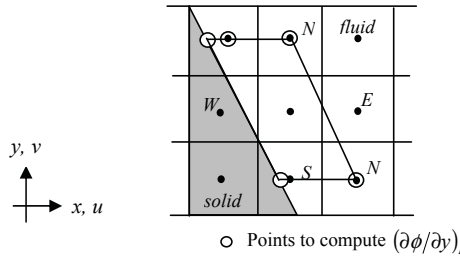


Figure 5: Points to compute  $(\partial\phi/\partial y)_I$ .

Similar to Eq. (8) can be obtained

$$a_P\phi_P = a_E\phi_E + a_W\phi_W + a_N\phi_N + a_S\phi_S + b^\phi \tag{21}$$

= for all control volumes described in Fig. 3. The coefficients,  $a_P$ ,  $a_E$ ,  $a_W$ ,  $a_N$ ,  $a_S$  and  $b^\phi$  are organized in Tabs. 1 to 3, including the first volume, which discretization already was described in this section.

For the coupling between pressure and velocity, the SIMPLEC algorithm (Semi Implicit Method for Pressure Linked Equations Consistent) was employed. The discretized equations are solved iteratively using the line-by-line method presented in Patankar (1980). Under-relaxation was employed to obtain a stable convergence for the solution of momentum and pressure equations.

Table 1: Coefficients for Eq. (21).

Cell	$a_p$	$a_E$	$a_W$	$a_N$	$a_S$
First	$a_E + a_N$	$D_e A( P_e ) + \langle -F_e, 0 \rangle$	0		0
Second	$a_E$	$D_e A( P_e ) + \langle -F_e, 0 \rangle$	0	0	0
Third	$a_E + a_N + a_S$	$D_e A( P_e ) + \langle -F_e, 0 \rangle$	0	$D_n A( P_n ) + \langle -F_n, 0 \rangle$	$D_s A( P_s ) + \langle F_s, 0 \rangle$
Fourth	$a_W + a_N$	0	$D_w A( P_w ) + \langle F_w, 0 \rangle$	$D_n A( P_n ) + \langle -F_n, 0 \rangle$	0
Fifth	$a_W$	0	$D_w A( P_w ) + \langle F_w, 0 \rangle$	0	0
Sixth	$a_W + a_N + a_S$	0	$D_w A( P_w ) + \langle F_w, 0 \rangle$	$D_n A( P_n ) + \langle -F_n, 0 \rangle$	$D_s A( P_s ) + \langle F_s, 0 \rangle$

Table 2: Source term, total and convective fluxes used in Tab. 1.

Cell	$b^\phi$	$J$	$F$
First	$\bar{S}^\phi - (J_{nw} - F_{nw}\phi_p) + (J_s - F_s\phi_p) - \Gamma_I^\phi \frac{\partial \phi}{\partial n} \Big _I dl_I$	$F_n \phi_n - \Gamma_n^\phi \frac{\partial \phi}{\partial y} \Big _n dl_n$	$\rho v dl \Big _n$
Second	$\bar{S}^\phi - \Gamma_I^\phi \frac{\partial \phi}{\partial n} \Big _I dl_I - (J_n - F_n\phi_p) + (J_s - F_s\phi_p)$ ,	$F_{ne} \phi_{ne} - \Gamma_{ne}^\phi \frac{\partial \phi}{\partial y} \Big _{ne} dl_{ne}$	$\rho v dl \Big _{ne}$
Third	$\bar{S}^\phi - (J_{nw} - F_{nw}\phi_p) + (J_{sw} - F_{sw}\phi_p) - \Gamma_I^\phi \frac{\partial \phi}{\partial n} \Big _I dl_I$	$F_{nw} \phi_{nw} - \Gamma_{nw}^\phi \frac{\partial \phi}{\partial y} \Big _{nw} dl_{nw}$	$\rho v dl \Big _{nw}$
Fourth	$\bar{S}^\phi - (J_{ne} - F_{ne}\phi_p) + (J_s - F_s\phi_p) + \Gamma_I^\phi \frac{\partial \phi}{\partial n} \Big _I dl_I$ ,	$-F_s \phi_s + \Gamma_s^\phi \frac{\partial \phi}{\partial y} \Big _s dl_s$	$\rho v dl \Big _s$
Fifth	$\bar{S}^\phi + \Gamma_I^\phi \frac{\partial \phi}{\partial n} \Big _I dl_I - (J_n - F_n\phi_p) + (J_s - F_s\phi_p)$ ,	$-F_{se} \phi_{se} + \Gamma_{se}^\phi \frac{\partial \phi}{\partial y} \Big _{se} dl_{se}$	$\rho v dl \Big _{se}$
Sixth	$\bar{S}^\phi - (J_{ne} - F_{ne}\phi_p) + (J_{se} - F_{se}\phi_p) - \Gamma_I^\phi \frac{\partial \phi}{\partial n} \Big _I dl_I$	$-F_{sw} \phi_{sw} + \Gamma_{sw}^\phi \frac{\partial \phi}{\partial y} \Big _{sw} dl_{sw}$	$\rho v dl \Big _{sw}$

Table 3: Variable  $\phi$  and  $(\partial \phi / \partial y)$ .

Faces	$\phi$	$(\partial \phi / \partial y)$
$n$	$c_1 x_n^2 y_n + c_2 x_n^2 + c_3 x_n y_n + c_4 x_n + c_5 y_n + c_6$	$c_1 x_n^2 + c_3 x_n + c_5$
$ne$	$c_1 x_{ne}^2 y_{ne} + c_2 x_{ne}^2 + c_3 x_{ne} y_{ne} + c_4 x_{ne} + c_5 y_{ne} + c_6$	$c_1 x_{ne}^2 + c_3 x_{ne} + c_5$
$nw$	$c_1 x_{nw}^2 y_{nw} + c_2 x_{nw}^2 + c_3 x_{nw} y_{nw} + c_4 x_{nw} + c_5 y_{nw} + c_6$	$c_1 x_{nw}^2 + c_3 x_{nw} + c_5$
$s$	$c_1 x_s^2 y_s + c_2 x_s^2 + c_3 x_s y_s + c_4 x_s + c_5 y_s + c_6$	$c_1 x_s^2 + c_3 x_s + c_5$
$se$	$c_1 x_{se}^2 y_{se} + c_2 x_{se}^2 + c_3 x_{se} y_{se} + c_4 x_{se} + c_5 y_{se} + c_6$	$c_1 x_{se}^2 + c_3 x_{se} + c_5$
$sw$	$c_1 x_{sw}^2 y_{sw} + c_2 x_{sw}^2 + c_3 x_{sw} y_{sw} + c_4 x_{sw} + c_5 y_{sw} + c_6$	$c_1 x_{sw}^2 + c_3 x_{sw} + c_5$

### 3 Numerical Results

In this section is presented flow patterns and characteristic parameters for a triangular cavity flow with different Reynolds numbers. Numerical tests for a variety of triangular geometries have been investigated, but for brevity, only give here the description for the equilateral cavity. Using Cartesian grids  $30 \times 60$ ,  $60 \times 120$ ,  $120 \times 240$ , and  $240 \times 480$ , we obtain numerical results for Reynolds number up to 1. The comparison between the coarse and fine grids in terms of accuracy of numerical results and computational time show the reliability using a coarse grid, formed by  $120 \times 240$  control volumes. Detailed characteristics parameters are given in Tab. 4. It can be seen from Tab. 4 that our results are in good agreement with those

obtained by Li e Tang (1996) and McQuain et al. (1994). In Tab. 4 the stream function (maximum),  $\psi$ , and vorticity,  $\zeta$ , values are presented at the center of the primary vortex.

To verify the accuracy of the results presented in Tab. 4 it was computed the absolute error,  $|\phi_p - \phi_o|$ , where the subscript  $p$  denotes the present work and the subscript  $o$  denotes the study made by other authors. Comparing the values of the stream function, the biggest error was obtained to  $Re = 200$ , with the value of 3.3% compared to Li and Tang (1996) and the smallest error was obtained to  $Re = 1$  with the value of 0.4% compared to McQuain *et al.* (1994). Comparing the values of vorticity the biggest error was obtained to  $Re = 200$  with the value of 2.69% compared to Li and Tang (1996) and smallest error was obtained to  $Re = 1$  with the value of 0.5% compared to Li and Tang (1996). The order of the errors obtained shown that the method employed in the present study is suitable to solve triangular cavity flow with reasonable accuracy.

Table 4: Stream function and vorticity values at the center of the primary vortex, for  $Re \leq 1500$ .

$Re$	Fontes	$\psi$	$\zeta$	$x$	$y$	Error $\psi$	Error $\zeta$
1	Present work	0.229	1.373	1.732	2.475		
	Li and Tang (1996)	0.235	1.368	1.767	2.460	0.006	0.005
	McQuain <i>et al.</i> (1994)	0.233	1.363	1.749	2.460	0.004	0.010
50	Present work	0.230	1.399	1.876	2.475		
	Li and Tang (1996)	0.240	1.527	2.113	2.460	0.010	0.128
	McQuain <i>et al.</i> (1994)	0.237	1.464	2.078	2.445	0.007	0.065
100	Present work	0.231	1.409	1.963	2.463		
	Li and Tang (1996)	0.253	1.349	2.044	2.340	0.022	0.060
	McQuain <i>et al.</i> (1994)	0.247	1.373	2.061	2.355	0.016	0.036
200	Present work	0.236	1.481	2.107	2.438		
	Li and Tang (1996)	0.269	1.212	1.940	2.280	0.033	0.269
	McQuain <i>et al.</i> (1994)	0.260	1.272	1.940	2.280	0.024	0.209
350	Present work	0.241	1.405	2.107	2.375		
	Li and Tang (1996)	0.277	1.124	1.905	2.220	0.036	0.281
	McQuain <i>et al.</i> (1994)	0.268	1.232	1.905	2.265	0.027	0.173
500	Present work	0.247	1.321	2.021	2.325		
	Li and Tang (1996)	0.279	1.066	1.871	2.160	0.032	0.255
	McQuain <i>et al.</i> (1994)	0.269	1.250	1.905	2.265	0.022	0.071
1000	Present work	0.252	1.200	1.934	2.275		
	Li and Tang (1996)	0.280	1.110	1.862	2.175	0.028	0.090
	McQuain <i>et al.</i> (1994)	-	-	-	-		

Properties of the center of the primary vortex, i.e., stream function and vorticity values are presented for Reynolds numbers 2000 to 6000 in Tab. 5, such results there are not in literature. Analytical study performed by Batchelor (1956) shows that the theoretical value of vorticity at the primary vortex center is 1.054 for equilateral cavity with length of side  $2\sqrt{3}$ . Our numerical results (see Tabs. 4 and 5) suggest that the stream function value at the center of the primary vortex,  $\psi$ , converges to a constant value, and its vorticity,  $\zeta$ , is quite close to 1.054 as  $500 \leq Re \leq 2000$ . Table 5 shows values to vorticity and stream function. Note that when  $Re$  is greater than 2000, the location of the center of the primary vortex seems to be independent of the Reynolds number.

Table 5: Stream function and vorticity values at the center of the primary vortex, for  $2000 \leq Re \leq 6000$ .

$Re$	$\psi$	$\zeta$	$x$	$y$
2000	0.239	1.070	1.905	2.238
3000	0.180	1.395	2.252	2.438
4000	0.160	1.436	2.338	2.475
5000	0.147	1.444	2.396	2.500
6000	0.138	1.435	2.425	2.512

In addition to local quantities, stream function and vorticity, it is interesting to compare global quantities as the total kinetic energy,  $E$ , and enstrophy,  $Z$ , defined by

$$E = \frac{1}{2} \int_{\Omega} \|U\|^2 dx, \quad (22)$$

$$Z = \frac{1}{2} \int_{\Omega} \|\zeta\|^2 dx, \quad (23)$$

where  $U_{i,j} = (u_{i,j}, v_{i,j})$ . In cavity flow the kinetic energy represents the total energy gained by system with the fluid displacement.

Table 6 presents the flow properties with the increasing Reynolds number from 1000 to 6000. Note that the location of the maximum stream function is the same location of the center of the primary vortex. As verified by Li and Tang (1996) it is observed that the interior of the primary vortex has almost constant vorticity for Reynolds number larger than 3000 (see Tab. 6). We can see that the total kinetic energy gives converged values and decreases with the Reynolds number while the enstrophy increases.

Table 6: Proprieties of flow in triangular cavity, for  $1000 \leq Re \leq 6000$ .

$Re$	Proprieties	Value	Location	
			$x$	$y$
1000	$\psi_{\max}$	0.252	1.934	2.275
	$\psi_{\min}$	-0.007	1.674	1.025
	$\zeta$	1.200	1.934	2.275
	$E$	0.235	-	-
	$Z$	15.139	-	-
2000	$\psi_{\max}$	0.239	1.905	2.238
	$\psi_{\min}$	-0.008	1.588	1.038
	$\zeta$	1.070	1.905	2.238
	$E$	0.211	-	-
	$Z$	16.568	-	-
3000	$\psi_{\max}$	0.180	2.252	2.438
	$\psi_{\min}$	-0.018	0.924	2.288
	$\zeta$	1.395	2.252	2.438
	$E$	0.136	-	-
	$Z$	18.250	-	-
4000	$\psi_{\max}$	0.160	2.338	2.475
	$\psi_{\min}$	-0.020	0.982	2.288
	$\zeta$	1.436	2.338	2.475
	$E$	0.113	-	-
	$Z$	19.197	-	-
5000	$\psi_{\max}$	0.147	2.396	2.5
	$\psi_{\min}$	-0.021	1.010	2.288
	$\zeta$	1.444	2.396	2.5
	$E$	0.099	-	-
	$Z$	19.989	-	-
6000	$\psi_{\max}$	0.138	2.429	2.512
	$\psi_{\min}$	-0.022	1.037	2.273
	$\zeta$	1.435	2.429	2.512
	$E$	0.089	-	-
	$Z$	20.676	-	-

Streamlines and vorticity contours are reported in Figs. 6 and 7, respectively, for  $Re = 1, 500, 1000, 2000, 3000, 4000, 5000$  and  $6000$ . The values used to plot the contours are described in Tab. 5. When the Reynolds number is small, the streamlines contour consists of one vortex only (see Fig. 6 to  $Re = 1$ ).

As the Reynolds number increases, first a secondary vortex and then a tertiary vortex arises, as we can see in Fig. 6. The size of the vortices depends on the Reynolds number too. In the triangular cavity, a major vortex is occupying the central part of the domain, while minor vortices appear at the lower corner, however when Reynolds number increases the lower vortices grow pushing the main vortex to the right part of the cavity.

The topmost vortex deviates from the center with increase in Reynolds number, since inertial effects near the top wall become more important as  $Re$  increases. For all Reynolds numbers, the lower vortices have their centers along the centerline of the cavity. The topmost vortex, where inertial effects are dominant, first moves to the right as  $Re$  increases and later moves back towards the center of the cavity, while the second vortex moves to the left and increases with the Reynolds number.

Plots of the contours of constant vorticity are shown in Fig. 7. It is seen that for small  $Re$ , the vorticity field is symmetrical about the centerline. However, as  $Re$  increases, the vorticity variation moves to the boundary regions of the cavity, while the interior or the topmost vortex tends to attain constant vorticity.

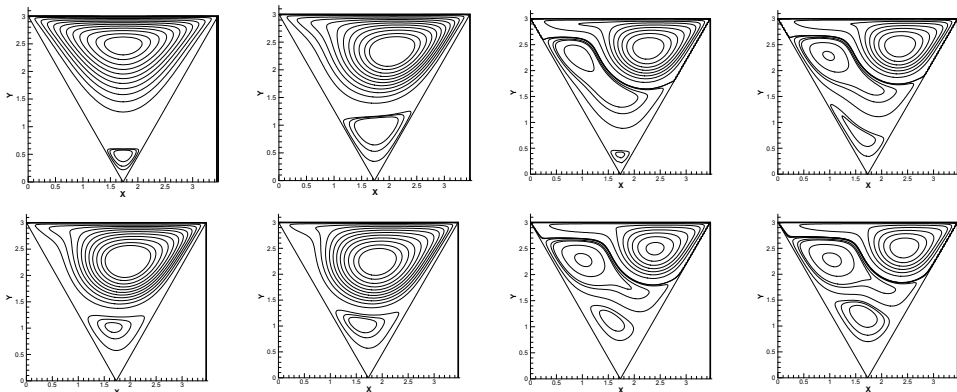


Figure 6: Streamlines for different Reynolds numbers.

#### 4 Conclusions

In this paper was presented the results of a steady viscous flow in a triangular cavity. With the use of Cartesian grids and an Eulerian-Lagrangian method, the solution was obtained without encountering any difficulties. The present approach proved to be quite successful and yielded accurate solutions for high Reynolds numbers, from 1 to 6,000. The numerical results obtained in this study were compared with results

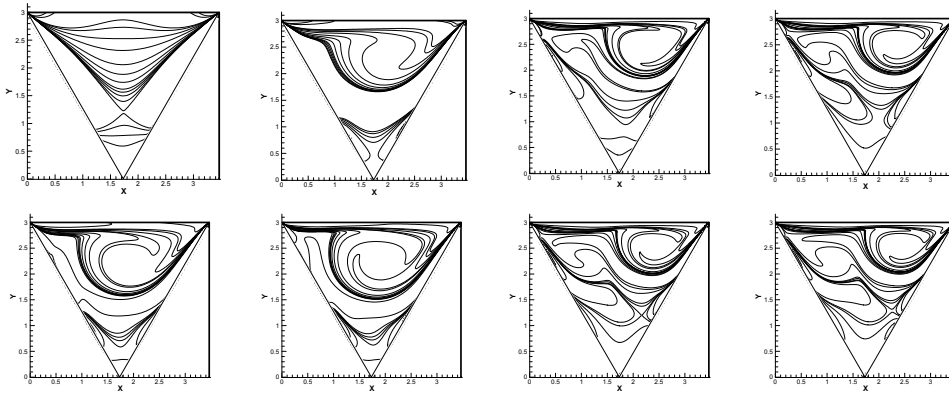


Figure 7: Vorticity contours for different Reynolds numbers.

reported in literature (Li and Tang, 1996; McQuain et al., 1994) and the agreement is good. The total kinetic energy gives converged values and decreases with the Reynolds number while the enstrophy increases. The triangular cavity flow can be a benchmark test case to study the performance of different numerical methods in irregular geometries.

**Acknowledgement:** The present work was developed with financial support of Fundação Araucária (FA 44/07 P9130), and the first author thanks scholarship received by Pontifical Catholic University of Paraná.

## References

- Ahrem, R.; Beckert, A.; Wendland, H.** (2006): A meshless spatial coupling scheme for large-scale fluid-structure interaction problems, *CMES: Computer Modeling in Engineering & Sciences*, Vol 12, No. 2, pp. 121-136.
- Arefmanesh, A.; Najafi, M.; Abdi, H.** (2008): Meshless local Petrov-Galerkin method with unity test function for non-isothermal fluid flow, *CMES: Computer Modeling in Engineering & Sciences*, Vol. 25, No. 1, pp. 9-22.
- Atluri S. N.; Liu H. T.; Han Z. D.** (2006a): Meshless Local Petrov-Galerkin (MLPG) Mixed Finite Difference Method for Solid Mechanics, *CMES: Computer Modeling in Engineering & Sciences*, Vol. 15, No. 1, pp. 1-16.
- Atluri S. N.; Liu H. T.; Han Z. D.** (2006b): Meshless Local Petrov-Galerkin (MLPG) Mixed Collocation Method for Elasticity Problems, *CMES: Computer Modeling in Engineering & Sciences*, Vol. 14, No. 3, pp. 141-152.

- Batchelor, G. K.** (1956): On steady laminar flow with closed streamlines at large Reynolds number. *J. Fluid Mech.*, Vol. 1, pp. 177-190.
- Benjamin A. S.; Denny V. E.** (1979): On the convergence of numerical solutions for 2-D flows in a cavity at large Re, *Journal of Computational Physics*, Vol. 33, pp. 340-358.
- Botella, O.; Peyret, R.** (1998): Benchmark spectral results on the lid-driven cavity flow, *Computers & Fluids*, Vol. 27, No. 4, pp. 421-433.
- Bruneau, C.-H.; Saad, M.** (2006): The 2D lid-driven cavity problem revisited. *Computers & Fluids*, Vol. 35, No. 3, pp. 326-348.
- Chantasiriwan, S.** (2006): Performance of multiquadric collocation method in solving lid-driven cavity flow problem with low Reynolds number, *CMES: Computer Modeling in Engineering & Sciences* Vol. 15, No. 3, pp. 137-146.
- Darr, J. H.; Vanka, S. P.** (1991): Separated flow in a driven trapezoidal cavity. *Phys. Fluids A*, Vol. 3, No. 3, pp. 385-392.
- Ding, H.; Shu, C.; Yeo, K. S.; Xu, D.** (2006): Numerical computation of three-dimensional incompressible viscous flows in the primitive variable form by local multiquadratic differential quadrature method, *Comp. Methods in Appl. Mech. Engr.*, Vol. 195, No. 7-8, pp. 516-533.
- Duan, Y.; Liu, R.** (2007): Lattice Boltzmann simulations of triangular cavity flow and free-surface problems, *Journal of Hydrodynamics*, Vol. 19, No. 2, pp. 127-134.
- Ghia, U.; Ghia, K. N.; Shin, C. T.** (1982): High-re solutions for incompressible flow using the Navier-Stokes equations and multigrid method, *J. Comp. Phys.*, Vol. 48, pp. 387-411.
- Glowinski, R.; Guidoboni, G.; Pan, T. -W.** (2006): Wall-driven incompressible viscous flow in a two-dimensional semi-circular cavity, *Journal of Computational Physics*, Vol. 216, No. 1, pp. 76-91.
- Grimaldi A.; Pascazio G.; Napolitano M.** (2006): A parallel multi-block method for the unsteady vorticity-velocity equations, *CMES: Computer Modeling in Engineering & Sciences*, Vol 14, No. 1, pp. 45-56.
- Jyotsna, R.; Vanka, S. P.** (1995): Multigrid calculation of steady, viscous flow in a triangular cavity. *Journal of Computational Physics*, Vol. 122, No. 1, pp. 107-117.
- Li, M.; Tang, T.** (1996): Steady viscous flow in a triangular cavity by efficient numerical techniques, *Computers Math. Applic.*, Vol. 31, No. 10, pp. 55-65.
- Lin, H.; Atluri, S. N.** (2001): The meshless local Petrov-Galerkin (MLPG) method for solving incompressible Navier-Stokes equations, *CMES: Computer Modeling in Engineering & Sciences*, Vol. 2, No. 2, pp. 117-142.

- Mai-Cao, L.; Tran-Cong, T.** (2008): A meshless approach to capturing moving interfaces in passive transport problems, *CMES: Computer Modeling in Engineering & Sciences*, Vol. 31, No. 3, pp. 157-188.
- Mai-Duy N.; Tran-Cong T.** (2004): Boundary integral-based domain decomposition technique of Navier-Stokes equations. *CMES: Computer Modeling in Engineering & Sciences*, Vol. 6, No. 1, pp. 59-75.
- Mariani, V. C.; Alonso, E. E. M.; Peters, S.** (2008): Numerical results for a colocated finite-volume scheme on Voronoi meshes for Navier-Stokes equations. *CMES: Computer Modeling in Engineering & Sciences*, Vol. 29, No. 1, pp. 15-27.
- Mariani, V. C.; Prata, A. T.** (2008): A Eulerian-Lagrangian method applied to fluid flow in lid-driven cavities with irregular bottom walls. *Numer. Heat Transfer Part B*, Vol. 53, No. 3, pp. 1-28.
- McQuain, W. D.; Ribbens, C. J.; Wang, C.-Y.; Watson, L. T.** (1994): Steady viscous flow in a trapezoidal cavity. *Comput. Fluids*, Vol. 23, No. 4, pp. 613-626.
- Moffatt H. K.** (1963): Viscous and resistive eddies near a sharp corner, *J. Fluid Mech.*, Vol. 18, No. 1, pp. 1-18.
- Nicolás, A.; Bermúdez, B.** (2004): 2D Incompressible viscous flows at moderate and high Reynolds numbers. *CMES: Computer Modeling in Engineering & Sciences*, Vol. 6, No. 5, pp. 441-451.
- Nicolás A.; Bermúdez, B.** (2007): Viscous incompressible flows by the velocity-vorticity Navier-Stokes equations, *CMES: Computer Modeling in Engineering & Sciences*, Vol 20, No. 2, pp. 73-83.
- Orsini, P.; Power, H.; Morvan, H.** (2008): Improving volume element methods by meshless radial basis function techniques, *CMES: Computer Modeling in Engineering & Sciences*, Vol. 23, No. 3, pp. 187-207.
- Patankar, S. V.** (1980): *Numerical heat transfer and fluid flow*, Hemisphere Publishing Corporation, USA.
- Ribbens, C. J.; Wang, C. -Y.; Watson, L. T.; Alexander, K. A.** (1991): Vorticity induced by a moving elliptic belt. *Comput. Fluids*, Vol. 20, No. 2, pp. 111-119.
- Ribbens, C. J.; Watson, L. T.; Wang, C. -Y.** (1994): Steady viscous flow in a triangular cavity. *J. Comput. Phys.*, Vol. 112, pp. 173-181.
- Vynnycky, M.; Kimura, S.** (1994): An investigation of recirculating in a driven cavity. *Phys. Fluids A*, Vol. 6, No. 11, pp. 3610-3620.
- Sellountos, E. J.; Sequeira, A.** (2008): A hybrid multi-region BEM/LBIE-RBF velocity-vorticity scheme for the two-dimensional Navier-Stokes equations. *CMES: Computer Modeling in Engineering & Sciences*, Vol. 23 No. 2, 127-147.

**Shan, Y. Y.; Shu, C.; Lu, Z. L.** (2008): Application of Local MQ-DQ Method to solve 3D incompressible viscous flows with curved boundary.

**Shyy, W.; Udaykumar, H. S.; Rao, M. M.; Smith, R. W.** (1996): *Computational Fluid Dynamics with Moving Boundaries*, Taylor & Francis, UK. *CMES: Computer Modeling in Engineering & Sciences*, Vol. 25, No. 2, 99-113.

**Tsai, C.; Young, D.L.; Cheng A.H.** (2002): Meshless BEM for Three-Dimensional Stokes Flows. *CMES: Computer Modeling in Engineering & Sciences*, Vol. 3, No. 1, 117-128.

**Udaykumar, H. S.; Shyy, W.; Rao, M. M.** (1996): ELAFINT: A mixed Eulerian-Lagrangian method for fluid flows with complex and moving boundaries, *Int. J. Numerical Methods in Fluids*, Vol. 22, No. 8, pp. 691-712.

**Ye, T.; Mittal, R.; Udaykumar, H. S.; Shyy, W.** (1999): An accurate Cartesian grid method for viscous incompressible flows with complex immersed boundaries. *J. Comp. Phys.*, Vol. 156, No. 2, pp. 209-240.

**Young, D. L.; Lane, S. C.; Lin, C. Y.; Chiu, C. L.; Chen, K. C.** (2004): Solutions of 2D and 3D Stokes laws using multiquadrics method. *Engr. Anal. With Bound. Elem.*, Vol. 28, No. 10, pp. 1233-1243.

**Han Z. D.; Liu H. T.; Rajendran A. M.; Atluri S. N.** (2006): The Applications of Meshless Local Petrov-Galerkin (MLPG) Approaches in High-Speed Impact, Penetration and Perforation Problems, *CMES: Computer Modeling in Engineering & Sciences*, Vol. 14, No. 2, pp. 119-128.

**Mai-Duy, N.; Mai-Cao, L.; Tran-Cong, T.** (2007): Computation of transient viscous flows using indirect radial basis function networks, *CMES: Computer Modeling in Engineering & Sciences*, Vol. 18, No. 1, pp. 59-78.

**Wen, P. H.; Hon, Y. C.** (2007): Geometrically Nonlinear Analysis of Reissner-Mindlin Plate by Meshless Computation, *CMES: Computer Modeling in Engineering & Sciences*, Vol. 21, No. 3, pp. 177-192.